Piezoelectrically Actuated Robotic System for MRI-Guided Prostate Percutaneous Therapy

Hao Su, *Member, IEEE*, Weijian Shang, *Student Member, IEEE*, Gregory Cole, *Member, IEEE*, Gang Li, *Student Member, IEEE*, Kevin Harrington, Alexander Camilo, Junichi Tokuda, Clare M. Tempany, Nobuhiko Hata, and Gregory S. Fischer, *Member, IEEE*

Abstract—This paper presents a fully actuated robotic system for percutaneous prostate therapy under continuously acquired live magnetic resonance imaging (MRI) guidance. The system is composed of modular hardware and software to support the surgical workflow of intraoperative MRI-guided surgical procedures. We present the development of a 6-degree-of-freedom (DOF) needle placement robot for transperineal prostate interventions. The robot consists of a 3-DOF needle driver module and a 3-DOF Cartesian motion module. The needle driver provides needle cannula translation and rotation (2-DOF) and stylet translation (1-DOF). A custom robot controller consisting of multiple piezoelectric motor drivers provides precision closed-loop control of piezoelectric motors and enables simultaneous robot motion and MR imaging. The developed modular robot control interface software performs image-based registration, kinematics calculation, and exchanges robot commands and coordinates between the navigation software and the robot controller with a new implementation of the open network communication protocol OpenIGTLink. Comprehensive compatibility of the robot is evaluated inside a 3-T MRI scanner using standard imaging sequences and the signal-to-noise ratio loss is limited to 15%. The image deterioration due to the present and motion of robot demonstrates unobservable image interference. Twenty-five targeted needle placements inside gelatin phantoms utilizing an 18-gauge ceramic needle demonstrated 0.87-mm root-mean-square (RMS) error in 3-D Euclidean distance based on MRI volume segmentation of the image-guided robotic needle placement procedure.

Index Terms—Biopsy, brachytherapy, image-guided therapy, MRI-guided robotics, piezoelectric actuation.

H. Su and G. Cole were with the Automation and Interventional Medicine Robotics Lab, Department of Mechanical Engineering, Worcester Polytechnic Institute. They are now with Philips Research North America, Briarcliff Manor, NY 10510 USA (e-mail: haosu.ieee@gmail.com).

W. Shang, G. Li, K. Harrington, A. Camilo, and G. S. Fischer are with the Automation and Interventional Medicine Robotics Lab, Department of Mechanical Engineering, Worcester Polytechnic Institute, Worcester, MA 01609 USA.

J. Tokuda, C. M. Tempany, and N. Hata are with the National Center for Image Guided Therapy, Brigham and Women's Hospital, Department of Radiology, Harvard Medical School, Boston, MA 02115 USA.
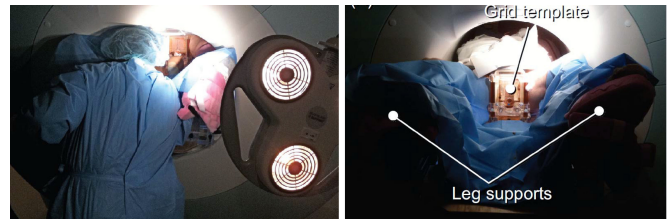
Fig. 1. (Left) A radiologist reaching the perineum of the patient inside closed-bore MRI while unable to see the navigation software, and (right) a mechanical grid template to guide manual needle placement. Figures are adapted from [2].

I. INTRODUCTION

MAGNETIC resonance imaging (MRI) offers high-resolution tissue imaging at arbitrary orientations and is also able to monitor therapeutic agents, surgical tools, tissue properties, and physiological function, which make MRI uniquely suitable for guiding, monitoring, and controlling a wide array of localized interventions [1]. Nevertheless, the limited space inside the bore is typically 60–70 cm in diameter and 170 cm in length. The ergonomics of manual needle placement prove very difficult in the confines of the scanner bore. Fig. 1 (left) shows a radiologist reaching into the center of the scanner bore to perform a needle placement through the perineum of a patient, and illustrates the challenging ergonomics of this manual insertion scenario.

A. Robot-Assisted Prostate Interventions With MRI Guidance

Numerous studies [3], [4] have shown that transrectal ultrasound (TRUS)-guided prostate biopsy, the most common approach to sample suspicious prostate tissue, provides relatively low quality images of the tissue and needles, and thus has limited ability to localize brachytherapy seeds, especially if there is a shadowing effect in a dense distribution of seeds. Due to concerns about MRI safety and compatibility of instrumentation, MRI is not, at this point, commonplace for guiding prostate cancer procedures.

To overcome the aforementioned challenges, robotics has been introduced. In the order of increased active actuation DOFs, early MRI-guided prostate interventional systems start from template-guided manual straight needle placement with transperineal approach as a proof of concept [5] at Brigham and Women's Hospital. Fig. 1 (right) shows a patient lying on a MRI scanner table with leg supports during the clinical case. Beyersdorff *et al.* [6] reported transrectal needle biopsies in

clinical studies employing 4-DOF passive alignment (rotation, angulation, and two linear translations) of a needle sleeve (Invivo Corp., USA). Krieger *et al.* presented a 3-DOF passive arm and a 2-DOF motorized arm to aim a needle guide for transrectal prostate biopsy [7]. Song *et al.* [8] developed 2-DOF motorized smart template guide consisting of vertical and horizontal crossbars that are driven by ultrasonic motors. Stoianovici *et al.* [9] described a pneumatic stepper motor and applied it to a new generation of robotic prostate interventions [10]. Our previous work presented a pneumatic servo system and sliding mode control [11] which was later adapted as a parallel manipulator for position-based teleoperation [12].

B. Robotic Actuation in the MRI Environment

Following the definition by American Society for Testing Materials (ASTM) standard F2503-05, in 2008, the U.S. Food and Drug Administration redefined the classifications of MRI devices as "MR Safe," "MR Conditional," and "MR Unsafe," while the term "MR Compatible" was not redefined and is not used in current standards. The latest ASTM F2503-13 clearly defines "MR Safe" as *"composed of materials that are electrically nonconductive, nonmetallic, and nonmagnetic."* Therefore, the proposed robot, like all electromechanical systems, strives for demonstrating *"safety in the MR environment within defined conditions"* and the "MR Conditional" classification. Note that these terms are about safety but neither image artifact nor device functionality is covered. *This manuscript demonstrates that the proposed robot is both safe in the MR environment in the intended configuration and that it does not significantly adversely affect image quality.*

From an actuation perspective, hydraulic actuation provides large power output and could be potentially MR Safe, but it is not ideal due to cavitation and fluid leakage [13]. Pneumatic actuation inherently could be designed intrinsically MR Safe. Thus, far only the transperineal access robot [9] and transrectal access robot [10] by Stoianovici *et al.* at the Johns Hopkins University and the robot by Yakar *et al.* [14] at the Radboud University Nijmegen Medical Center have proven to be completely MR Safe. A major issue of actuating with pneumatic cylinders is to maintain stability, which may result in overshooting due to the nonlinear friction force and long pneumatic transmission line induced slow response. Yang *et al.* [15] identified that the peak-to-peak amplitude of the oscillations before stabilization at the target location ranges in 2.5–5 mm with sliding mode control. Our experience with a pneumatic robotic using sliding mode control [11] demonstrated 0.94 mm RMS accuracy for a single axis. Alternatively, current pneumatic stepper motors achieve 3.3° [9] and 60° step size [16] demonstrating limited positioning capability.

Piezoelectric actuators can be very compact, provide submicron precision, and good dynamic performance without overshooting. Compared with pneumatics, piezoelectricity have unparalleled positioning accuracy and power density [17]. For example, the rotary piezoelectric motor in our robot (PiezoLegs, LR80, PiezoMotor AB, Sweden) has a 5.73×10^{-6} degree step angle and is 23-mm diameter by 34.7 mm long, as compared

with the novel pneumatic stepper motor described in [18] with a 3.3° step angle and is $70 \times 20 \times 25$ mm. However, piezoelectric motors utilizing commercially available motor drivers cause unacceptable MR imaging noise (up to 40–80% signal loss) during synchronous robot motion [7]. In previous work, Fischer and Krieger *et al.* evaluated various types and configurations of piezoelectric actuation options demonstrating the limitations of commercially available piezoelectric drive systems [20]. *A primary contribution of this paper is "minimizing" the image artifact caused by standard motor drivers and enable high-performance motion control through development of a custom control system and leveraging the advantages of these actuators through design of a piezoelectrically-actuated robot.* A historical review of MRI-guided robotics and the challenges related to piezoelectric actuation can be found in [13], [20], and [21].

C. Contribution

Generally, previous work in MRI-guided prostate intervention utilizing piezoelectric actuation is limited in the following three aspects. First, a majority of the previously developed systems are not fully actuated; thus, remains time-consuming and necessitating moving the patient inside the scanner for imaging and moving the patient out of the scanner bore for the interventional procedure. Second, robots utilizing commercially available drivers have to interleave motion with imaging [22] to prevent electrical noise that causes 40–80% signal degradation [7], precluding real-time MR image guidance. Third, most of the prior research systems are either scanner-dependent (i.e., they require specific electrical, mechanical, and/or software interfaces to a scanner model/vendor or scanner room, or they are not readily transported and setup for use in an arbitrary MRI scanner), or they are platform dependent (e.g., based on a specific control interface [23]), or lack integrated navigation, communication, visualization, and hardware control.

Hence, the primary contributions of the paper are: 1) a fully actuated 6-DOF robot capable of performing both prostate biopsy and brachytherapy procedures with MR image guidance, while keeping the patient inside the MRI bore; 2) a feature-rich motion control system capable of effectively driving piezoelectric motors during real time continuously acquired 3-T MRI imaging; 3) a modular hardware (robotic manipulator and the control system) and software (image processing, semi-autonomous robot control, registration, and navigation) system that supports network communication and is also readily extendable to other clinical procedures; and 4) a vendor-neutral and scanner room-independent system. This paper demonstrates evaluation with a Philips Achieva 3-T scanner; similar results have been identified with Siemens Magnetom 3-T MRI scanner [24].

II. DESIGN REQUIREMENTS AND SYSTEM ARCHITECTURE

A. System Concept and Specifications

The prostate interventional robot design aims to model the procedure after a radiologist's hand motion and fit between
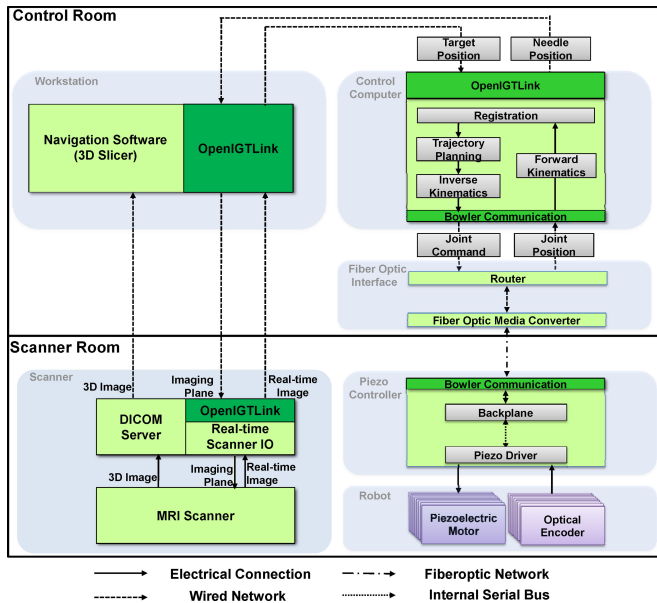
Fig. 2. System architecture and data flow of the robotic system. Six modules are shown in gray block and OpenIGTLink is used to exchange control, image, and position data.

patient legs inside an MRI scanner bore. Beyond the compatibility with the MRI environment, the following are the primary design considerations.

1) *Workspace:* The patient lies inside MRI scanner in the semilithotomy position, and the robot accesses the prostate through the perineal wall. The typical prostate is 50 mm in the lateral direction by 35 mm in the anterior-posterior (AP) direction by 40 mm in length. To cover all volume of prostate and accommodate patient variability, the prostate is assumed to have the shape of a sphere with 50-mm diameter. Thus, the required motion range is as follows: vertical motion of 50 mm (100–150 mm above the scanner bed surface), lateral motion of ±25 mm from the center of the workspace, and needle insertion depth is 150 mm to reach the back of the prostate from the skin entry point at the perineum.

2) *Sterilizability:* Only the plastic needle guide, collet, nut, and guide sleeve have direct contact with the needle or the patient and are removable and sterilizable. The remainder of the robot can be draped with a sterilized plastic cover.

B. System Architecture

The system architecture comprises the following six modules depicted in Fig. 2: 1) a needle placement robot inside MRI scanner; 2) a piezoelectric robot controller inside MRI scanner room, 3) an interface box with a fiber optic media converter and router; 4) a control computer running robot control software; 5) surgical planning, navigation, and visualization software 3D Slicer; and 6) an MRI scanner and image acquisition interface. The system is designed from the ground up to be modular, readily reconfigurable, and scanner independent. The hardware architecture enables scanner independence by only requiring a

grounded ac socket in the scanner room and a waveguide tube to pass out a fiber optic cable. There is no requirement for specific patch panel configurations, which may not have the required connections (or must be customized), may allow noise to pass into the scanner room, and often have filters that degrade (or completely prevent) piezoelectric motor diver signals from passing. The control system is modular in the sense that communication between all modules (except the one between robot controller and robot itself which are adjacent) is through a network connection as indicated with dashed lines, which implies that not only each module's computational platforms but also programming languages are not required to be identical.

Surgical navigation software 3D Slicer, serves as a user interface for the surgeon. The system workflow follows a preoperative planning, fiducial frame registration, targeting, and verification procedure as presented in Section V. OpenIGTLink [25] is used to exchange control, position, and image data. The details of the module design are described in the following sections.

Communication from the control computer (inside the console room) to the robot controller (inside scanner room) is through fiber optic Ethernet running through a readily available waveguide tube in the patch panel. Computer control signals and joint positions are communicated through fiber optic conversion between MRI scanner room and console room, eliminating any electrical signal passing in/out of the scanner room and, thus, a large source of noise that is introduced when electrical signal passes through the patch panel or wave guide since the cables act as antennas to induce stray RF noise.

III. MECHANISM DESIGN

This new design has been significantly improved over our prior work [26] with increased structural rigidity, mechanical reliability, and ease of assembly. The major construction components of the robot (e.g., motor fixture and belt tensioner) are made with fused deposition modeling (Dimension 1200es, Stratasys, Inc., USA) and polyjet 3-D printing (Objet Connex260, Stratasys, Inc., USA). Plastic bearings and aluminum guide rails (Igus Inc., USA) are used in the transmission mechanisms. Optical encoders (U.S. Digital, USA) with PC5 differential line drivers that have been shown to cause no visible MRI artifact when appropriately configured are used for position encoding [11].

Clinical brachytherapy and biopsy needles are composed of two concentric shafts, an outer hollow cannula and an inner solid stylet. Eighteen-gauge needles are typically used for clinical prostate brachytherapy, and radioactive seeds are typically preloaded with spacers between them, often 5.5 mm apart. Straight needle placement typically includes three decoupled tasks: 1) moving the needle tip to the entry point with 3-DOF Cartesian motion; 2) inserting the needle into the body using 1-DOF translation along a straight trajectory; and 3) firing the spring loaded mechanism of the biopsy gun to harvest tissue or retracting the stylet for placing radioactive seeds. These three tasks are implemented with two modules as described in the section that follows. The described device is a unified mechanism
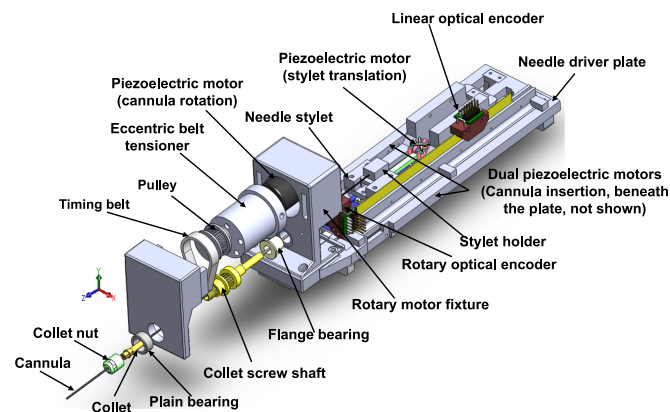
Fig. 3.   Exploded view of the needle driver module, including a rotary axis, a translation axis, and a collinear stylet translation axis.
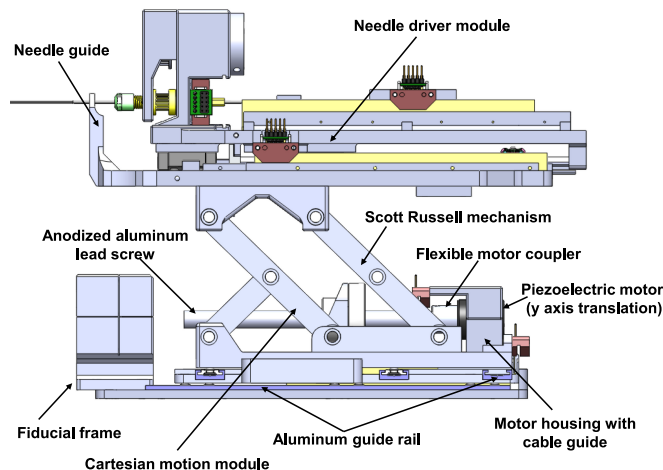

Fig. 4.   Side view of the 3-DOF needle driver module providing cannula translation and rotation (2-DOF) and stylet translation (1-DOF) and the 3-DOF actuated Cartesian stage module.

capable of being configured for the two separate procedures of biopsy and brachytherapy.

A. Needle Driver Module

For transperineal prostate needle placement, which requires 18-N force to puncture the capsule of the prostate [27], dual linear piezoelectric motors (PiezoLegs LL1011C, PiezoMotor AB, Sweden), each providing 10 N holding force and 1.5 cm/s speed are placed in parallel to drive 1-DOF insertion motion. This mechanism design is illustrated in Fig. 3; these motors are not clearly visible since they are placed beneath the needle driver plate. Another 1-DOF of collinear translational stylet motion is driven by another PiezoLegs actuator to coordinate the motion with respect to the cannula. For biopsy, the firing motion is also implemented as rapid cannula-stylet coordinated motion using the same coaxial mechanism. This idea unifies the two procedures and simplified mechanism design.

The needle driver's design allows standard needles with different diameters, ranging from 25 (0.51-mm diameter) to 16 gauge (1.65-mm diameter) to be used. A collet clamping device rigidly couples the cannula shaft (outer needle) to the driving motor mechanism as shown in Fig. 3. The clamping device is connected to the rotary motor through a timing belt. A plastic bushing with an eccentric extruded cut is used as pulley tensioner, where the extruded cut is used to house a rotary piezo-electric motor (PiezoLegs, LR80, PiezoMotor AB, Sweden). Rotation of the belt tensioner can adjust the distance between the motor shaft and the collet shaft of clamping mechanism. In the previous robot iteration [26], collet screw shaft bending was observed and the mechanism has been significantly improved with a newly designed tensioner that includes a shaft support with plain bearing to prevent motor shaft bending. The plastic needle guide with a press-fit quick release mechanism, collet nut, and guide sleeve that have direct contact with the needle are, therefore, readily detachable and sterilizable.

B. Cartesian Motion Module

The needle driver is placed on top of a 3-DOF Cartesian positioning module shown in Fig. 4. The mechanism design was developed in a decoupled manner, thus the kinematics are simple and safe by separating the alignment and insertion motions. The horizontal 2-DOF motions are achieved using the same linear motors with direct drive. Motion in the vertical plane enables 40 mm of vertical travel. To increase rigidity of the vertical mechanism over the previous prototype [26], [28] that has a single scissor mechanism, the new design utilized a one-and-half Scott-Russell scissor mechanism which is compact and attenuates structural flexibility due to plastic bars and bearings as identified in Fig. 4. Vertical motion is achieved by actuating this mechanism with a aluminum anodized lead screw (2-mm pitch). The piezoelectric motors exhibit inherent braking when not actively driven providing further safety.

The piezoelectric motors used here are capable of micrometer level positioning accuracy, and the limiting factor is the closed-loop position sensor. The optical encoders in this robot have encoding resolution of 0.0127 mm/count (EM1-0-500-I) and 0.072°/count (EM1-1-1250-I) for linear and rotary motion, respectively.

IV. ELECTRICAL DESIGN

A. Piezoelectric Motors

Piezoelectric motors are one of the most commonly utilized classes of actuators in MRI-guided devices, as they operate on the reverse piezoelectric effect without a magnetic field as required by traditional motors. In terms of driving signal, piezo-electric motors fall into two main categories: harmonic and nonharmonic. Both have been demonstrated to cause interference within the scanner bore with commercially available drive systems [7]. While these motors operate on similar basic principles, signals required to effectively utilize and control them are quite different. Harmonic motors, such as Nanomotion motors (Nanomotion Ltd., Israel), are generally driven with fixed frequency sinusoidal signal on two channels at 38–50 kHz and velocity control is through amplitude modulation of 80–300 V RMS. Shinsei harmonic motors (Shinsei Corporation, Japan),

however, are speed controlled through frequency modulation. Nonharmonic motors, such as PiezoLegs motors, operate at a lower frequency (750–3000 Hz) than harmonic motors. These actuators require a complex-shaped waveform on four channels generated with high precision at fixed amplitude (typically a low voltage of < 50 V), and speed is controlled through modulating the drive frequency.

B. Piezoelectric Motor Driver and Control

Though there have been efforts to shield motors (such as with RF shielding cloth) and ground the shielded control cables (e.g., the most recent one from Krieger *et al.* [7]), the MRI compatibly results demonstrate that signal-to-noise ratio (SNR) reduction is up to 80%. From our prior study [19], the source of noise is primarily from the driving signal rather than the motor itself. Commercially available piezoelectric motor drivers typically use a class-D style amplification system that generates the waveforms by low-pass filtering high-frequency square waves. By using switching drivers (the typical approach since the manufacturers primary design goal was power efficiency instead of noise reduction), significant RF emissions and noise on the motor drive lines are introduced which cause interference with imaging as demonstrated in [7] and [19] and in many other works. Although filtering can improve the results, it has not been effective in eliminating the interference and often significantly degrades motor performance.

This manuscript describes our implementation of a piezoelectric motor driver with signals generated from a direct digital synthesizer (DDS), high-performance multichannel digital-to-analog converter (DAC), high power linear amplifiers, and π filtered outputs. In contrast to commercial drivers based on high-frequency switching voltage regulators, it is capable of cleanly generating both high-voltage sinusoidal signals and low voltage precise waveforms such that it could be used to drive both harmonic (e.g., Shinsei and Nanomotion) and nonharmonic (e.g., PiezoLegs) commercial motors [24]. A block diagram of the driver, shown in Fig. 5, is based on linear amplifiers with very high speed DACs that allow precise waveform shape control while eliminating any unwanted noise (both by defining a smooth waveform and through the circuit design including isolation, filtering, and shielding), thus fundamentally addressing the driving signal-induced image interference.

PiezoLegs motors were the actuators of choice in this robot and, therefore, are the focus of the detailed discussion and evaluation. They consist of four quasi-static legs (A, B, C, and D legs) forming a stator which interchangeably establish frictional contact to a ceramic drive preloaded with a beryllium copper leaf spring, and are operated below their resonant frequency. Each bimorph leg consists of two electrically isolated piezoelectric stacks. The legs elongate when an equal voltage is applied to the two stacks of one leg. Applying different voltages on the two stacks of one leg causes the leg to bend.

As shown in Fig. 5, the developed custom motor driver utilizes a microcontroller (PIC32MX460F512L, Microchip Tech.) and a field-programmable gate array (FPGA, Cyclone EP2C8Q208C8, Altera Corp.). The functionality of the micro-
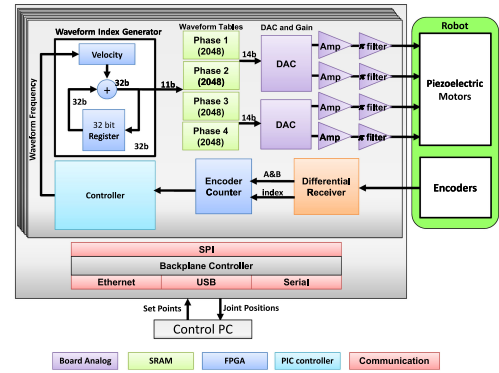

Fig. 5. Block diagram of the system components of each piezoelectric motor driver board. An FPGA is configured as a waveform synthesizer generating the four phases of the drive signal which are passed to a linear amplifier stage with integrated filtering.

controller includes: 1) loading waveform from SD card to the internal RAM of FPGA; 2) communication with PC through Ethernet to receive position or velocity set points; 3) real-time position and velocity servo control loops. The microcontroller incorporates a joint-level controller that controls the output sample rate of the FPGA's waveform synthesizer. The functionality of the FPGA includes: 1) DDS; 2) encoder decoding, where differential encoder signals pass through a differential receiver for improved robustness to noise, are interpreted by the FPGA, and are fed to on-board microcontroller; 3) overheat and fault protection. An internal temperature sensor in the motor amplifier (OPA549, Texas Instruments, USA) is used to manage thermal shutdown of the output; 4) stall and limit detection. The system allows the control PC to communicate with the driver in three ways: Ethernet, universal serial bus (USB), and serial communication—in this application, Ethernet is used. Communication with the robot controller between driver boards utilized a serial peripheral interface (SPI) bus. A watchdog mechanism detects the stall motion of the motor after 5-ms time out as a safety mechanism during joint limit detection and the homing procedure. To drive the motor, arbitrary-shaped waveforms provided by the manufacturer are resampled and loaded onto the SD card. One pair of legs (A and C legs) typically has the same waveform, while the other pair (B and D legs) uses the same waveform with $90°$ phase shift. The DDS on the FPGA generates these four waveforms and the signal frequency is expressed as

$$ \mathrm{F} = \frac{M}{2^n} F_{\mathrm{clock}} \tag{1} $$

where M is the frequency control tuning word from the microcontroller, n is the bit of phase accumulator (32 bit), and F_{clock} is the clock frequency (50 MHz). For a desired frequency, the corresponding M is calculated in the FPGA. A 32-bit register in the FPGA is used as phase accumulator (shown as blue block

in Fig. 5) to produce the digital phase, whose top 11 bits are used as an index to the 11-bit waveform table (2048 element long lookup table, shown as green block in Fig. 5) that maps the phase to corresponding waveform.

The generated digital waveform is converted to an analog signal through a pair of two-channel high speed DACs (DAC2904, Texas Instruments, USA) shown as purple block in Fig. 5. The driver boards include a high power output amplification module, which passes the signals from four linear amplifiers to the actuators through high efficiency π filters to further remove the high-frequency noise. This module includes three stages of linear amplifiers in sequence.

As shown in (2), a variation of a discrete nonlinear proportional integral derivative controller is implemented in microcontroller to control the motor motion. Since these piezoelectric motors have inherent breaking, high bandwidth, and low inertia, damping with a derivative term is typically not required for smooth motion with no overshoot

$$
u = \begin{cases} 0, & |e| \le \mathrm{d} \\ k_p e + k_i \int e\, dt \subseteq [\mathrm{f}_{\min}, \mathrm{f}_{\max}], & \mathrm{d} < e < l \\ u_{\max}, & e \ge l \end{cases} \quad (2)
$$

where, u is the control signal, e is the position error, $f_{\min}$ and $f_{\max}$ are the minimum (750 Hz) and maximum (3 kHz) driving frequencies, respectively. k_p and k_i are the PI control parameters, although k_d is implemented, it is set to zero and, therefore, left out of this equation. d and l are the minimum and maximum position threshold values for linear frequency control. d is the dead-band and it is set to one encoder tick to eliminate chatter; it is implemented inside the FPGA running at 50 MHz and is capable of stopping the low inertia motors at the setpoint almost instantaneously. $u_{\max}$ is saturation that ensures the motor to run at the specified maximum velocity associated with $f_{\max}$ when the position error is greater than a predetermined value. To maintain high-speed motion while not damaging the motor, the control frequency is limited by minimum speed (which should be reached at the target) and maximum speed (which it should never exceed). k_p is tuned to be large to allow the motor to run at the capped maximum speed until very close to the target.

Fig. 6 shows the portable shielded aluminum robot controller enclosure which houses the custom-made piezoelectric motor driver boards configured for up to eight-axis control. A key step in reducing image degradation from electrical noise is to encase all electronics in a continuous Faraday cage to block as much electromagnetic interference being emitted from the equipment as possible. This cage is extended through the shielded cables carrying electrical signals out of the cage through serpentine wave guides located on the vertical sides of the control box. Standard 120 V AC power is filtered and passes to a linear regulator with 48 V DC output which provides power to the piezoelectric motor drivers and additional regulators to generate lower voltage power for the control electronics.
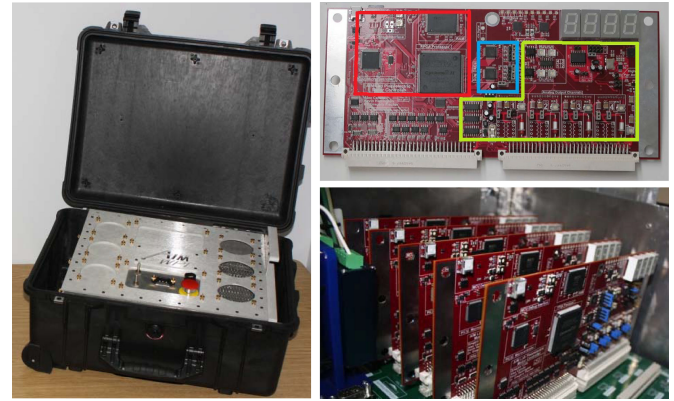

Fig. 6. (Left) MRI robot controller enclosed inside a carry on travel case. (Right) Piezoelectric motor controller. Red box shows the digital control section with microcontroller for closed-loop control and FPGA for waveform synthesis. Blue box shows the high speed parallel DACs and preamplifier circuits. Yellow box shows the high power filtered linear amplifier stage.
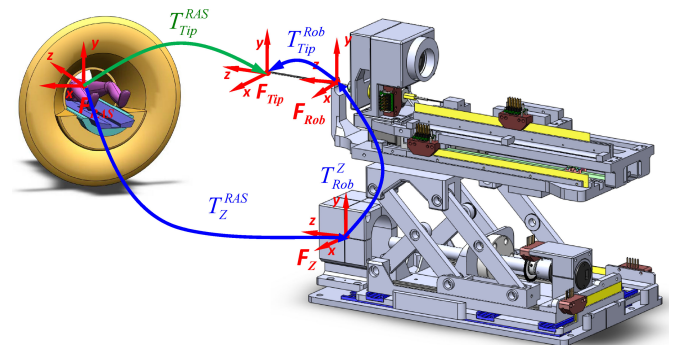

Fig. 7. Coordinate frames of the robotic system for registration of the robot to MR image space, robot kinematics, and encoded needle insertion.

V. Registration, Control Software, and Workflow

The primary functionality of the robot control interface software developed as a part of this paper is to enforce and integrate the system workflow, including fiducial registration, robot registration, kinematics, and motion control. The robot control interface software connects navigation software to the robot controller to exchange robot commands using the OpenIGTLink protocol. Three-dimensional surgical navigation software 3D Slicer serves as a user interface to visualize and define target in image space; however, the modular system may be readily adapted to other platforms.

A. Surgical Navigation Coordinates

The robot is registered to the patient coordinate system (referred to as right-anterior-superior (RAS) coordinates) based on imaging a fiducial frame (referred to as the Z-frame) attached to the robot as shown in Fig. 7. Details of the multislice-based fiducial registration can be found in our recent work [29]; this evaluation of registration accuracy showed subpixel resolution with a mean error of 0.27 mm in translation and $0.16°$ in orientation.

After the registration phase, the robot can accept target coordinates represented in RAS image coordinates.

The corresponding series of homogeneous transformations is used to determine the robot's tip location in MR image coordinates (i.e., RAS coordinates)

$$T_{\text{Tip}}^{\text{RAS}} = T_{Z}^{\text{RAS}} \cdot T_{\text{Rob}}^{Z} \cdot T_{\text{Tip}}^{\text{Rob}} \tag{3}$$

where $T_{\text{Tip}}^{\text{RAS}}$ is the needle tip in the RAS patient coordinate system, T_{Z}^{RAS} is the fiducial's 6-DOF coordinate in RAS coordinates as determined by the Z-frame fiducial-based registration, T_{Rob}^{Z} is the robot needle guide location with respect to the robot base (coincident with fiducial's 6-DOF coordinate) as determined from the forward kinematics of the robot as defined in Section V-B, and $T_{\text{Tip}}^{\text{Rob}}$ is the needle tip position with respect to the front face of the needle guide (typically at the skin entry point) of the robot as measured by optical encoder along the needle insertion axis.

B. Robot Kinematics

With the navigation coordinate relation, we can substitute the kinematics into the kinematic chain to calculate the needle tip position and orientation. The vertical motion of the robot is provided by actuation of the scissor mechanism. A linear motion in the superior-inferior direction produces a motion in the AP direction. The forward kinematics of the robot with respect to the fiducial frame is defined as

$$
\begin{aligned}
x &= q_1 + x_{\text{offset}} \\
y &= \sqrt{L^2 - (\text{L} - d)^2} + y_{\text{offset}} \\
z &= q_3 + q_4 + z_{\text{offset}}
\end{aligned} \tag{4}
$$

where $d = \frac{q_2 \cdot p}{360}$ is the horizontal linear motion of the lead screw due to the rotary motor motion and p is the lead screw pitch. q_1, q_2, q_3, q_4 are joint space motion of the x-axis motor translation (unit: mm), y-axis rotary motor ration (unit: degree), z-axis motor translation (unit: mm), and needle driver insertion translation (unit: mm). L is the length of the scissor bar. The three offset terms in (4) are corresponding to the homogeneous transformation matrix T_{Rob}^{Z} in (3). q_4 is corresponding to the transformation $T_{\text{Tip}}^{\text{Rob}}$ and the remainder of (4) is corresponding to the transformation T_{Rob}^{Z}.

C. Control Software for Communication and Kinematics

The control software is transparent to clinician and is developed for communication and kinematics computation based on the calculation from the last sections. A robot kinematics and OpenIGTLink communication library was developed in Java with a graphical user interface (GUI) that coordinates system input, communication, and procedure workflow, while the clinician interfaces with the higher level navigation software (e.g., 3D Slicer). As shown in Fig. 8, the technical/engineering GUI for the robot control application based upon the developed Java library includes four major modules. 1) Robot registration and calibration module (upper left column). It displays the registration matrix T_{Z}^{RAS} and matrix T_{Rob}^{Z}. 2) The upper middle column
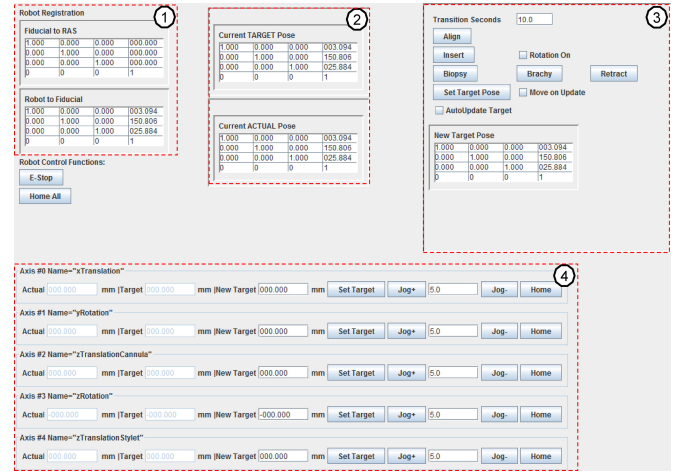

Fig. 8. GUI of the robot control software running on the control computer in control room. The upper left column (1) is robot registration and calibration, the upper middle column (2) displays the current target point transformation and current actual robot 6-DOF pose. The upper right column (3) contains the desired target transformation and buttons to control biopsy or brachytherapy procedures. The bottom row (4) is the joint space panel.

displays the current target and current actual 6-DOF pose as homogeneous transformation matrices. 3) The upper right column contains a homogeneous transformation representing the desired new target. Additional buttons are included to control biopsy or brachytherapy procedure steps. 4) The bottom row is the joint space panel which is automatically generated for a robot mechanism configuration through an extensible markup language (XML) configuration file containing the name of each joint, the actual joint position, the desired joint position, motor jogging, and home buttons.

D. Clinical Software and Workflow

On top of the control software, a clinical software module was developed in 3D Slicer to manage clinical workflow and communicate with robot and imaging workstation. A virtual needle of the clinical software module accepts the pose information through OpenIGTLink from the robot and displays with MRI volume to assure placement safety and confirm placement accuracy as shown in Fig. 9, where the yellow spheres indicate the selected targets inside MRI volume in RAS coordinates.

The workflow mimics traditional TRUS-guided prostate insertions. The system components of the control software follow the workflow and enable the following five phases.

1) *System Initialization:* The hardware and software system is initialized. In this phase, the operator prepares the robot by connecting the robot controller and attaching sterilized needle and needle attaching components to the robot. The robot is calibrated to a predefined home position and loads the robot configuration from the XML file.
2) *Planning:* Preoperative MR images are loaded into 3D Slicer and targets are selected or imported.
3) *Registration:* A series of transverse images of the fiducial frame are acquired. Multiple images are used to perform multislice registration to enhance system accuracy.
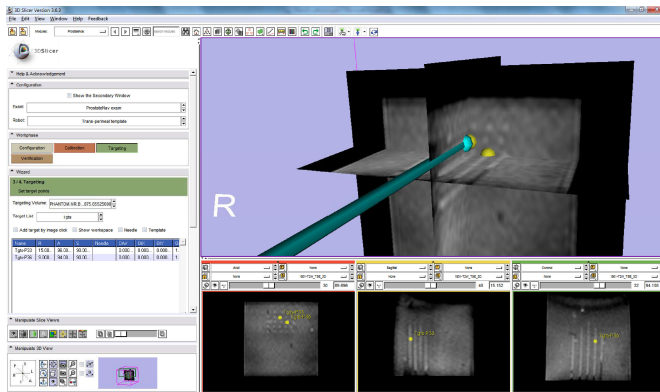
Fig. 9. Clinical GUI integrated inside 3D Slicer shows a virtual needle whose position was streamed from control software was inserted to move to the selected targets (shown as yellow spheres) during needle placement accuracy evaluation. The needle tracks were visualized inside the MRI volume. The first column of the bottom subfigures shows the 5×5 needle tracks.

4) *Targeting:* Needle target is selected from 3D Slicer and this desired position is transmitted to the robot to process inverse kinematics and the calculated joint command is used to drive piezoelectric motors. Targets or adjustments may also be directly entered or adjusted in the robot control interface software. Real-time MR images can be acquired during insertion that enables visualization of the tool path in MRI with the overlaid reported robot position.

5) *Verification:* The robot forward kinematics calculate actual needle tip position (from encoder measurements and registration results) which is displayed in 3D Slicer. Postinsertion MR images are acquired and displayed with overlaid target and actual robot position.

VI. EXPERIMENTS AND RESULTS

To demonstrate compatibility with the MRI environment and accuracy of the robotic system, comprehensive MRI phantom experiments were performed. Imaging quality and needle placement accuracy were systematically analyzed.

A. MR Image Quality Evaluation

We evaluated compatibility of the needle placement robot in a Philips Achieva 3-T system. This evaluation includes two assessments to quantify the image quality: 1) *SNR ratio analysis* based on National Electrical Manufacturers Association (NEMA) standard MS1-2008; and 2) *image deterioration factor analysis* based on the method in [30]. The analysis utilized a periodic image quality test (PIQT) phantom (Philips, Netherlands) that has complex geometric features, including uniform cylindrical cross section, and arch/pin section. The robot is placed in close proximity (5 mm) to the phantom. The controller was placed approximately 2 m away from the scanner bore inside the scanner room. Fig. 10 (first row) shows the system setup.

The image quality analysis was performed with four imaging protocols shown in Table I (the first three is for quantitative analysis with a phantom and the fourth is for qualitative assessment with a human volunteer): 1) diagnostic imaging
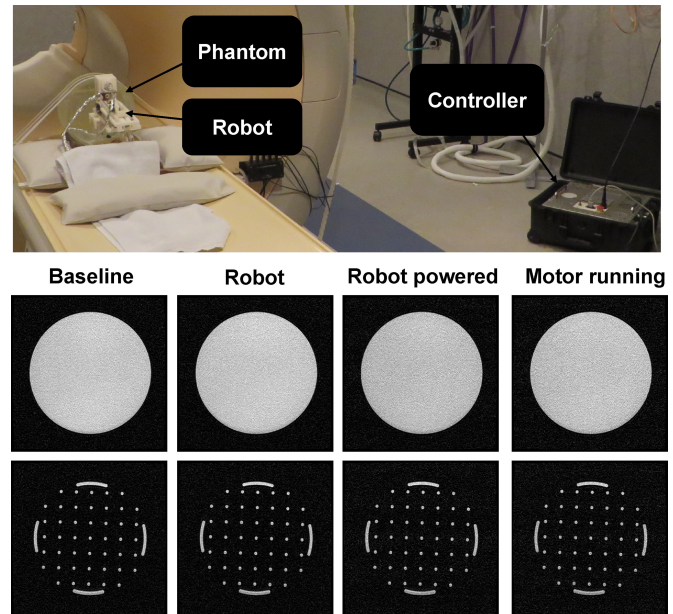

Fig. 10. (First row) The robot prototype configuration in a 3-T MRI scanner with a feature-rich PIQT phantom for the evaluation studies. (Second row) Representative T1W-FFE images of the cylindrical cross section for each of four configurations. (Third row) Corresponding T1W-FFE images of the arch/pin cross sections.

TABLE I
SCAN PARAMETERS FOR COMPATIBILITY EVALUATION

Protocol	TE (ms)	TR (ms)	FA (deg)	Slice (mm)	Bandwidth (Hz/pixel)
T1W-FFE	2.3	225	75	2	1314
T2W-TSE-Planning	90	4800	90	3	239
T2W-TSE-Needle	115	3030	90	3	271
T2W-TSE-Prostate	104	4800	90	3	184

T1-weighted fast field echo (T1W-FFE); 2) diagnostic imaging T2-weighted turbo spin echo for initial surgical planning scan (T2W-TSE-Planning); 3) diagnostic imaging T2-weighted turbo spin echo for needle confirmation (T2W-TSE-Needle); and 4) a standard T2-weighted prostate imaging sequence (T2W-TSE-prostate). All sequences were acquired with field of view 256 mm $\times$ 256 mm, 512×512 image matrix, and 0.5 mm $\times$ 0.5 mm pixel size.

Four configurations were evaluated for SNR analysis: 1) baseline of the phantom only; 2) robot present but controller and robot power off (controller power is the power from ac socket and robot power is controlled by emergency stop); 3) controller and robot powered; and 4) motor powered on and robot is in motion during imaging. Fig. 10 (second row) illustrates the representative images of SNR test with T1W-FFE images in the different configurations.

The following imaging sets were acquired twice for each imaging sequence in the Philips 3-T scanner to calculate the image deterioration factors:

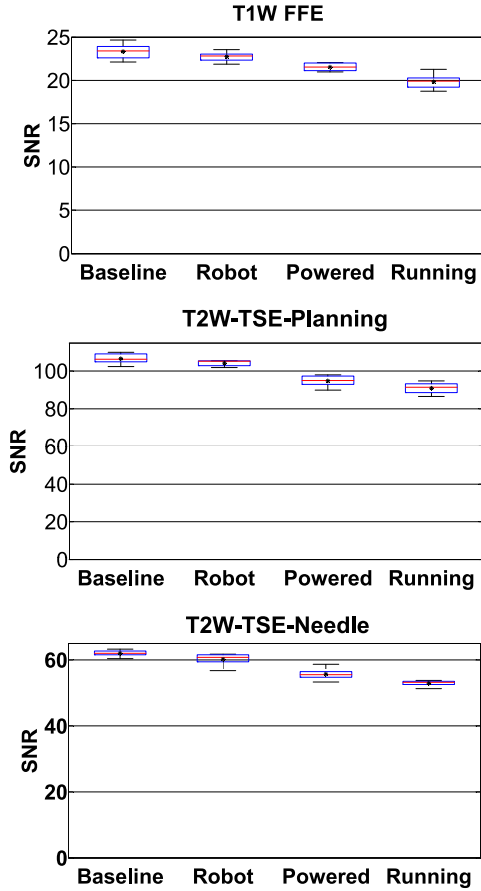1) *Baseline (BL1 and BL2):* baseline image of the phantom without the robot;

Fig. 11. Boxplot of the SNR for four robot configurations under three scan protocols. The "*" represents the mean SNR, the horizontal line in the middle of the box represents the median, the top and bottom represent the quartiles, and the whiskers represent the limits.

TABLE II
MEAN SNR CHANGE IN DIFFERENT CONFIGURATIONS

Protocol	Baseline	Robot Present (%Change)	Powered (%Change)	Motor Running (%Change)
T1W-FFE	23.32	22.735 (2.79%)	21.54 (7.63%)	19.86 (14.87%)
T2W-TSE-Planning	106.69	104.27 (2.27%)	94.80 (11.14%)	90.96 (14.74%)
T2W-TSE-Diagnosis	61.98	60.19 (2.89%)	55.65 (10.23%)	52.91 (14.64%)

2) *Robot Present (RO1 and RO2):* image of the phantom with the robot in place, powered off;
3) *Robot Motion (RM1 and RM2):* image of the phantom with the robot in motion.

For statistical analysis, SNR based upon the NEMA standard definition is utilized as the metric for evaluating MR image quality. SNR was calculated as the mean signal in the center of the phantom divided by the noise outside the phantom. Mean signal is defined as the mean pixel intensity in the region of interest. The noise is defined as the average mean signal intensity in the four corners divided by 1.25 [31]. In Fig. 11, the boxplot shows the variation in SNR for images taken in each configuration for the three imaging sequence. The change of SNR mean value is shown in Table II.
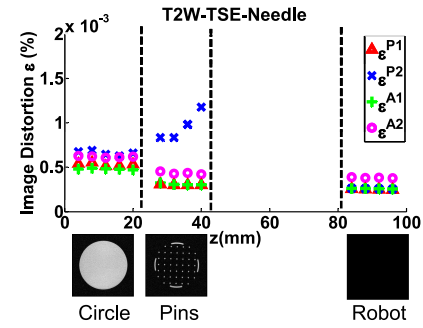

Fig. 12. Passive (P) and active (A) image deterioration factor ε variation due to the present and motion of the robot.

TABLE III
DETERIORATION FACTOR FOR PASSIVE AND ACTIVE TESTS

Protocol	E_P %	E_A %
T1W-FFE	0.000015	0.00012
T2W-TSE-Planning	0.00139	0.00019
T2W-TSE-Diagnosis	0.00036	0.00013

Although SNR analysis shows promising result, it cannot fully characterize the property of image deterioration. Therefore, image deterioration analysis [30] was conducted to establish a quantitative image deterioration metric due to the present of the robot in the imaging field (E_P—passive test) and by the robot motion (E_A—active test). As defined in [30], measures $E_P \leq 2\%$ and $E_A \leq 1\%$ are associated with unobservable image interference. Utilizing the same notation [30], T notates passive or active configuration set. The error ϵ^{T1} reflects the normal level of noise from the imaging system itself. The factors E_P and E_A indicate the image deterioration due to materials in the passive test (P) and the electronics in the active test (A), respectively. Similar to Stoianovici *et al.* [10]:

1) ϵ^{P1} reflects differences between two sets taken without the robot (BL1-BL2);
2) ϵ^{P2} reflects differences between two sets taken without and with the robot (BL1-RO1), a representation of the materials-induced image deterioration;
3) ϵ^{A1} reflects differences between two sets taken with the robot present and without robot motion (RO1-RO2);
4) ϵ^{A2} reflects differences between two sets taken with the robot present (no motion) and with robot motion (RO1-RM1), a representation of the electronics-induced image deterioration.

Fig. 12 shows the plot of one representative protocol (T2W-TSE-Diagnosis) with these parameters. The average difference between ϵ^{P2} and ϵ^{P1} produces the passive image deterioration factor E_P, and the average difference between ϵ^{A2} and ϵ^{A1} produces the active factor E_A. Their experimental values are shown in Table III.

Based on the promising qualitative analysis of the robotic system, it was furthered evaluated with human prostate anatomy. A healthy volunteer lay in the semilithotomy position and was imaged with T2W-TSE-Prostate protocol in Table I. Fig. 13 depicts
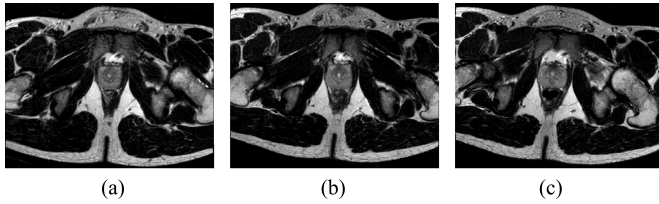
Fig. 13. MRI images of human prostate under different conditions: baseline, without robot (a), controller present and unpowered (b), and robot running (c).

the MR images under each of the conditions: baseline, without robot, controller present and power off, and robot running.

The major observations from these two quantitative and one qualitative evaluation include:

1) the different imaging sequences demonstrated similar behavior SNR reduction. This is also observed in [7];
2) the present of the robot with power off introduces 2.79%, 2.27%, and 2.89% SNR reduction for T1W-FFE, T2W-TSE-Planning, and T2W-TSE-Diagnosis, respectively. This reflects the material caused SNR reduction;
3) the SNR reduction in the configuration of the robot powered but not running (7.63%, 11.14%, and 10.23% for each sequence) is less than that the motor running (14.87%, 14.74%, and 14.64%). This reflects the electrical noise caused SNR reduction. In comparison, the mean SNR of baseline and robot motion during T1 imaging by Krieger *et al.* [7], reduced approximately from 250 to 50 (80%), while it changed from 380 to 70 (72%). Our system shows significant improvement over [7] that utilized commercial motor drivers when the robot was in motion. As shown in Figs. 10 and 13, there is no readily visible difference;
4) the deterioration factor shows unobservable interference for all protocols in all configurations tested, according to the requirement $E_P \leq 2\%$ and $E_A \leq 1\%$ [30].

B. Phantom-Based Accuracy Evaluation of Multiple Needle Placements in MRI

Joint space accuracy has been evaluated in [32] demonstrating an average 0.03 mm tracking accuracy with the piezoelectric motors. The robot was further evaluated in a phantom study under MR imaging. The phantom used for the experiments was muscle-like ballistic test media (Corbin Inc., USA). The rubber-like material was molded into a 10 cm × 10 cm × 15 cm rectangular form. This phantom was placed inside a standard flex imaging coil configuration, and the robot was initialized to its home position in front of the phantom similar to that shown in Fig. 10.

The goal of this trial was to assess the robot's inherent accuracy and, therefore, the authors strove to limit paramagnetic artifact of the needles, which would affect assessment of the robot's accuracy. Clinical MRI needles are typically made of titanium, which still produces a needle track artifact greater than the actual needle size; therefore, 18-gauge ceramic needles were inserted into a gelatin phantom to assess robot instrument tip po-
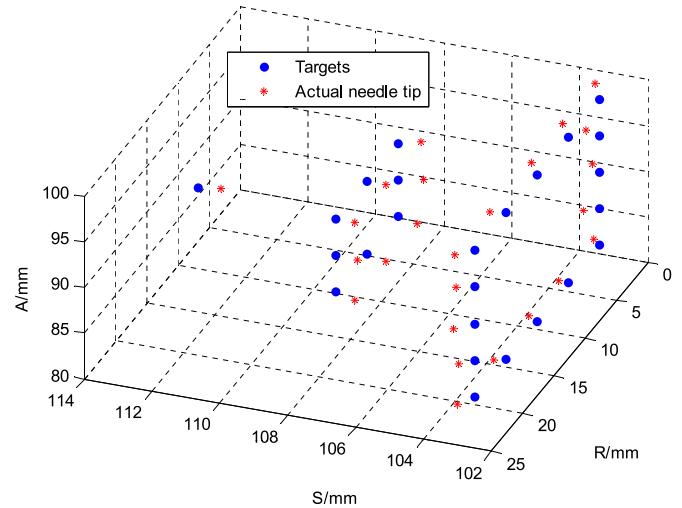

Fig. 14. Twenty-five targets forming a semi ellipse to simulate the superior part of a prostate were selected from the MRI volume. Actual needle tip position determined from segmented MRI image are superimposed with the 25 targets.

sition. The ceramic needle was custom made from ceramic rods (Ortech Ceramics, USA) and the tip was ground to symmetric diamond shape with a $60°$ cone shape. In the clinical procedures, 18-gauge needle made of low artifact titanium (Invivo Corp, USA) are typically used.

T2W-TSE-Diagnosis is utilized to visualize the needle insertion trajectory. 25 needle placement targets (virtual targets specified in MRI volume) that form a semiellipsoid shape are selected from the MRI volume, as shown in Fig. 14. The transverse plane distance of the grid is 5 mm to mimic a mechanical template of TRUS procedure. Needles were inserted without using the needle rotation motion to demonstrate the robot accuracy independent of additional control methods that may further be used to improve accuracy.

Needle placement accuracy was evaluated along each direction as shown in Fig. 15. The actual needle tip position is manually segmented from postinsertion MRI volume images. The desired targets and the needle tip positions were registered with point cloud to cloud registration. The maximum error is less than 1.2 mm as shown in Fig. 15 and it indicates a consistent accuracy trend of the image-guided robotic system. The RMS error as calculated with 3-D Euclidean distance between the desired and actual needle tip position is 0.87 mm with a standard deviation of 0.24 mm, which is on par with the MR image resolution.

VII. DISCUSSION AND CONCLUSION

This paper presents a fully-actuated robotic system for MRI-guided prostate interventions using piezoelectric actuation. In this paper, we developed and evaluated an integrated modular hardware and software system to support the surgical workflow of intraoperative MRI, with percutaneous prostate intervention as an illustrative case. Extensive compatibility experiments have been conducted to quantitatively evaluate the SNR reduction and image deterioration factor and qualitatively the image quality of
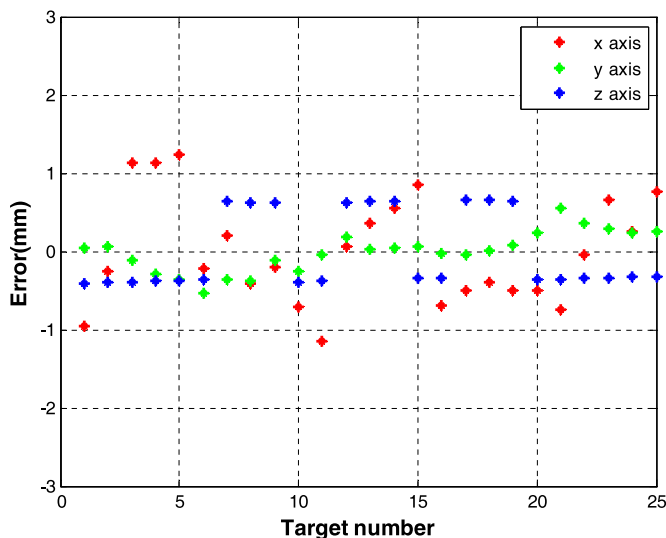
Fig. 15.   Needle placement errors of 25 targeted needle placements along *x-y-z* axis components with the 3-D Euclidean distance RMS error 0.87 mm.

human prostate tissue. Since the latest ASTM F2503-13 standard requires only fully nonconductive components to be considered "MR Safe," this system (based upon piezoelectric actuation which still relies on electrical currents and wires) has been demonstrated to be "MR Conditional" which indicates that it is safe in the intended configuration. The SNR analysis and image deterioration analysis experiments with the complex phantom demonstrate that this robotic system causes no major image artifacts or distortion, paving for the route to regulatory clearance. Phantom experiments validated the capability of the system to execute actuated prostate biopsy placement, and the spacial accuracy is 0.87 mm $\pm$ 0.24 mm. In comparison with pneumatics, Yang *et al.* [15] reported 2.5–5 mm-oscillations for each axis with sliding mode control. Our pneumatic robotic system with sliding mode control [11] demonstrated 0.94-mm RMS accuracy for single axis. The piezoelectric actuation demonstrate a clear advantage over the pneumatic counterpart. Since this motor is capable of micrometer level accuracy, encoder resolution is the effective limit. For our application, 0.03 mm single joint motion accuracy is more than sufficient. In general, the root cause of needle placement error is from two sources, namely the needle-caused error and robotic system itself. Even though our transperineal approach with MRI guidance can avoid the TRUS probe-induced prostate motion and deformation, needle-caused error includes prostate translation, rotation, and deformation during needle insertion, needle deflection due to needle tissue interaction, and susceptibility artifact shift of needle due to titanium or nickel titanium material of the needle itself. In terms of the robot-related error, it includes the error from fiducial registration and intrinsic error of the manipulator itself due to positioning accuracy of the motor, structure flexibility, and misalignment. In this paper, we aim to isolate the targeting accuracy of the robotic system by utilizing virtual targets and ceramic needles. So the error in this experiment reflects the accumulation of errors due to the robot positioning limitation,

image-based registration, and needle deflection, excluding the error due to susceptibility artifact shift or organ motion.

Future work would focus on addressing the related issues including utilizing more rigid material (e.g., ultem and PEEK rather than ABS and acrylic), using needle rotation during insertion to decrease deflection, and modeling susceptibility artifact. As the 3-D position of the needle is available, we can dynamically adjust the scan plane of MRI to visualize needle insertion process, which could be used to track needle trajectory to increase the safety and accuracy.

REFERENCES

[1] F. A. Jolesz, "Intraoperative imaging in neurosurgery: Where will the future take us?" in *Intraoperative Imaging*, ser. Acta Neurochirurgica Supplement, M. N. Pamir, V. Seifert, and T. Kiris, Eds. New York, NY, USA: Springer, 2011, pp. 21–25.

[2] J. Tokuda, K. Tuncali, I. Iordachita, S.-E. Song, A. Fedorov, S. Oguro, A. Lasso, F. M. Fennessy, C. M. Tempany, and N. Hata, "In-bore setup and software for 3T MRI-guided transperineal prostate biopsy," *Phys. Med. Biol.*, vol. 57, pp. 5823–5840, Sep. 2012.

[3] H. S. Bassan, R. V. Patel, and M. Moallem, "A novel manipulator for percutaneous needle insertion: Design and experimentation," *IEEE/ASME Trans. Mechatronics*, vol. 14, no. 6, pp. 746–761, Dec. 2009.

[4] N. Hungr, M. Baumann, J.-A. Long, and J. Troccaz, "A 3-D ultrasound robotic prostate brachytherapy system with prostate motion tracking," *IEEE Trans. Robot.*, vol. 28, no. 6, pp. 1382–1397, Dec. 2012.

[5] A. V. D'Amico, C. M. Tempany, R. Cormack, N. Hata, M. Jinzaki, K. Tuncali, M. Weinstein, and J. P. Richie, "Transperineal magnetic resonance image guided prostate biopsy," *J. Urology*, vol. 164, no. 2, pp. 385–387, Aug. 2000.

[6] D. Beyersdorff, A. Winkel, B. Hamm, S. Lenk, S. A. Loening, and M. Taupitz, "MR imaging-guided prostate biopsy with a closed MR unit at 1.5 T: Initial results," *Radiology*, vol. 234, no. 2, pp. 576–581, Feb. 2005.

[7] A. Krieger, S. Song, N. Bongjoon Cho, I. Iordachita, P. Guion, G. Fichtinger, and L. L. Whitcomb, "Development and evaluation of an actuated MRI-compatible robotic system for MRI-guided prostate intervention," *IEEE/ASME Trans. Mechatronics*, vol. 18, no. 1, pp. 273–284, Feb. 2013.

[8] S.-E. Song, J. Tokuda, K. Tuncali, C. Tempany, E. Zhang, and N. Hata, "Development and preliminary evaluation of a motorized needle guide template for MRI-guided targeted prostate biopsy," *IEEE Trans. Biomed. Eng.*, vol. 60, no. 11, pp. 3019–3027, Nov. 2013.

[9] D. Stoianovici, D. Song, D. Petrisor, D. Ursu, D. Mazilu, M. Muntener, M. Mutener, M. Schar, and A. Patriciu, "MRI stealth robot for prostate interventions," *Minimally Invasive Ther. Allied Technol.*, vol. 16, no. 4, pp. 241–248, 2007.

[10] D. Stoianovici, C. Kim, G. Srimathveeravalli, P. Sebrecht, D. Petrisor, J. Coleman, S. Solomon, and H. Hricak, "MRI-safe robot for endorectal prostate biopsy," *IEEE/ASME Trans. Mechatronics*, vol. 19, no. 4, pp. 1289–1299, Aug. 2014.

[11] G. S. Fischer, I. Iordachita, C. Csoma, J. Tokuda, S. P. DiMaio, C. M. Tempany, N. Hata, and G. Fichtinger, "MRI-compatible pneumatic robot for transperineal prostate needle placement," *IEEE/ASME Trans. Mechatronics*, vol. 13, no. 3, pp. 295–305, Jun. 2008.

[12] R. Seifabadi, S.-E. Song, A. Krieger, N. B. Cho, J. Tokuda, G. Fichtinger, and I. Iordachita, "Robotic system for MRI-guided prostate biopsy: Feasibility of teleoperated needle insertion and ex vivo phantom study," *Int. J. Comput. Aided Radiol. Surg.*, vol. 7, pp. 181–190, 2011.

[13] R. Gassert, A. Yamamoto, D. Chapuis, L. Dovat, H. Bleuler, and E. Burdet, "Actuation methods for applications in MR environments," *Concepts Magn. Reson. Part B, Magn. Reson. Eng.*, vol. 29B, no. 4, pp. 191–209, 2006.

[14] D. Yakar, M. G. Schouten, D. G. H. Bosboom, J. O. Barentsz, T. W. J. Scheenen, and J. J. Futterer, "Feasibility of a pneumatically actuated MR-compatible robot for transrectal prostate biopsy guidance," *Radiology*, vol. 260, no. 1, pp. 241–247, 2011.

[15] B. Yang, U.-X. Tan, A. B. McMillan, R. Gullapalli, and J. P. Desai, "Design and control of a 1-DOF MRI-compatible pneumatically actuated robot with long transmission lines," *IEEE/ASME Trans. Mechatronics*, vol. 16, no. 6, pp. 1040–1048, Sep. 2011.

[16] Y. Chen, C. Mershon, and Z. Tse, "A 10-mm MR-conditional unidirectional pneumatic stepper motor," *IEEE/ASME Trans. Mechatronics*, vol. PP, no. 99, pp. 1–7, 2014.

[17] J. Huber, N. Fleck, and M. Ashby, "The selection of mechanical actuators based on performance indices," in *Proc. Royal Soc. London. Ser. A, Math., Phys. Eng. Sci.*, vol. 453, no. 1965, pp. 2185–2205, 1997.

[18] D. Stoianovici, A. Patriciu, D. Petrisor, D. Mazilu, and L. Kavoussi, "A new type of motor: Pneumatic step motor," *IEEE/ASME Trans. Mechatronics*, vol. 12, no. 1, pp. 98–106, Feb. 2007.

[19] G. S. Fischer, A. Krieger, I. Iordachita, C. Csoma, L. L. Whitcomb, and G. Fichtinger, "MRI compatibility of robot actuation techniques— A comparative study," in *Proc. Int. Conf. Med. Image Comput. Comput. Assisted Intervention.*, Sep. 2008.

[20] H. Elhawary, Z. T. H. Tse, A. Hamed, M. Rea, B. L. Davies, and M. U. Lamperth, "The case for MR-compatible robotics: A review of the state of the art," *Int. J. Med. Robot. Comput. Assisted Surg.*, vol. 4, no. 2, pp. 105–113, 2008.

[21] J. J. Fütterer, S. Misra, and K. J. Macura, "MRI of the prostate: Potential role of robots," *Imaging*, vol. 2, no. 5, pp. 583–592, 2010.

[22] A. Goldenberg, J. Trachtenberg, W. Kucharczyk, Y. Yi, M. Haider, L. Ma, R. Weersink, and C. Raoufi, "Robotic system for closed-bore MRI-guided prostatic interventions," *IEEE/ASME Trans. Mechatronics*, vol. 13, no. 3, pp. 374–379, Jun. 2008.

[23] H. Elhawary, Z. Tse, M. Rea, A. Zivanovic, B. Davies, C. Besant, N. de Souza, D. McRobbie, I. Young, and M. Lamperth, "Robotic system for transrectal biopsy of the prostate: Real-time guidance under MRI," *IEEE Eng. Med. Biol. Mag.*, vol. 29, no. 2, pp. 78 –86, Mar. 2010.

[24] G. S. Fischer, G. A. Cole, and H. Su, "Approaches to creating and controlling motion in MRI," in *Proc. IEEE Annu. Int. Conf. Eng. Med. Biol. Soc.*, 2011, pp. 6687–6690.

[25] J. Tokuda, G. S. Fischer, X. Papademetris, Z. Yaniv, L. Ibanez, P. Cheng, H. Liu, J. Blevins, J. Arata, A. J. Golby, T. Kapur, S. Pieper, E. C. Burdette, G. Fichtinger, C. M. Tempany, and N. Hata, "OpenIGTLink: An open network protocol for image-guided therapy environment," *Int. J. Med. Robot. Comput. Assisted Surg.*, vol. 5, no. 4, pp. 423–434, 2009.

[26] H. Su, M. Zervas, G. Cole, C. Furlong, and G. S. Fischer, "Real-time MRI-guided needle placement robot with integrated fiber optic force sensing," in *Proc.IEEE Int. Conf.Robot. Autom*, 2011, pp. 1583–1588.

[27] Y. Yu, T. Podder, Y. Zhang, W. Ng, V. Misic, J. Sherman, L. Fu, D. Fuller, E. Messing, D. Rubens, J. Strang, and R. Brasacchio, "Robot-assisted prostate brachytherapy," *Med. Image Comput. Comput.-Assisted Intervention*, vol. 9, pp. 41–49, 2006.

[28] H. Su, D. Cardona, W. Shang, A. Camilo, G. Cole, D. Rucker, R. Webster, and G. Fischer, "MRI-guided concentric tube continuum robot with piezoelectric actuation: A feasibility study," in *Proc. IEEE Int. Conf. Robot. Autom.*, 2012, pp. 1939–1945.

[29] W. Shang and G. S. Fischer, "A high accuracy multi-image registration method for tracking MRI-guided robots," *Proc. SPIE Med. Imag.*, vol. 8316, 2012.

[30] D. Stoianovici, "Multi-imager compatible actuation principles in surgical robotics." *Int. J. Med. Robot. Comput. Assisted Surg.*, vol. 1, no. 2, pp. 86–100, Jan. 2005.

[31] *Determination of Signal-to-Noise Ratio (SNR) in Diagnostic Magnetic Resonance Imaging*, NEMA Standard Publication MS 1-2008, 2008.

[32] H. Su, W. Shang, K. Harrington, A. Camilo, G. A. Cole, J. Tokuda, C. Tempany, N. Hata, and G. S. Fischer. (2012), "A networked modular hardware and software system for MRI-guided robotic prostate interventions," *Proc. SPIE Med. Imag.*, vol. 8316, [online]. http://proceedings.spiedigitallibrary.org/proceeding.aspx?articleid=1285684.
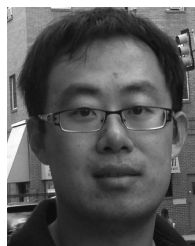
Hao Su (M'12) received the B.S. degree from the Harbin Institute of Technology and the M.S. degree in mechanical and aerospace engineering from the State University of New York, Buffalo, NY, USA, and received the Ph.D. degree in mechanical engineering from the Worcester Polytechnic Institute, Worcester, MA, USA.

He is currently a Research Scientist at Philips Research North America, Briarcliff Manor, NY, USA.

Dr. Su received the Best Medical Robotics Paper Finalist Award in the IEEE International Conference on Robotics and Automation. He received the Link Foundation Fellowship and Dr. Richard Schlesinger Award from the American Society for Quality.
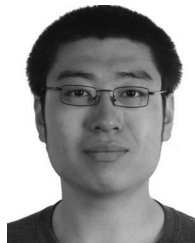
Weijian Shang (S'12) received the B.S. degree in precision instruments and mechanology from Tsinghua University, Beijing, China, in 2009, and the M.S. degree in mechanical engineering from Worcester Polytechnic Institute, Worcester, MA, USA, in 2012, where he is currently working toward the Ph.D. degree in mechanical engineering.

Gregory Cole (M'12) received the B.S. and M.S. degrees in mechanical engineering and the Ph.D. degree in robotic engineering in 2013 from Worcester Polytechnic Institute, Worcester, MA, USA.

He is currently a Research Scientist at Philips Research North America, Briarcliff Manor, NY, USA.

Gang Li (S'12) received the B.S. and M.S. degrees in mechanical engineering from the Harbin Institute of Technology, Harbin, China, in 2008 and 2011, respectively. He is currently working toward the Doctoral degree in the Department of Mechanical Engineering at Worcester Polytechnic Institute, Worcester, MA, USA.

Kevin Harrington received the B.S. degree in robotic engineering from Worcester Polytechnic Institute, Worcester, MA, USA.

He is currently with the Automation and Interventional Medicine Robotics Lab, Department of Mechanical Engineering, Worcester Polytechnic Institute.

Alexander Camilo received the B.S. degree in electrical and computer engineering from Worcester Polytechnic Institute, Worcester, MA, USA.

He is currently with the Automation and Interventional Medicine Robotics Lab, Department of Mechanical Engineering, Worcester Polytechnic Institute.

Junichi Tokuda received the B.S. degree in engineering, the M.S. and Ph.D degrees in information science and technology in 2002, 2004, and 2007, respectively, all from the University of Tokyo, Tokyo, Japan.

He is currently an Assistant Professor of Radiology at Brigham and Women's Hospital and Harvard Medical School, Boston, MA, USA.

Nobuhiko Hata received the B.E., M.E., and D.Eng. degrees in precision machinery engineering in 1993, 1995, and 1998, respectively, all from the University of Tokyo, Tokyo, Japan.

He is currently an Associate Professor of radiology at Harvard Medical School, Boston, MA, USA.

Clare M. Tempany received the MB BAO, BCh degrees from the Royal College of Surgeons, Dublin, Ireland.

She is currently the Ferenc Jolesz Chair and the Vice-Chair of Radiology Research, Department of Radiology, Brigham and Women's Hospital, Boston, MA, USA, and a Professor of Radiology at Harvard Medical School, Boston. She is also the Clinical Director of the National Image Guided Therapy Center.

Gregory S. Fischer (M'03) received the B.S. degree in electrical and mechanical engineering from Rensselaer Polytechnic Institute, Troy, NY, USA, and the M.S.E. degree in electrical engineering and the Ph.D. degree in mechanical engineering in 2008 from Johns Hopkins University, Baltimore, MD, USA.

He is currently an Associate Professor of mechanical engineering at Worcester Polytechnic Institute, Worcester, MA, USA, and is the Director of the WPI Automation and Interventional Medicine (AIM) Laboratory.